ADVANCED HEALTHCARE MATERIALS
www.advhealthmat.de

Check for updates

Biocompliant Composite Au/pHEMA Plasmonic Scaffolds for 3D Cell Culture and Noninvasive Sensing of Cellular Metabolites

*Sean E. Lehman, Joselle M. McCracken, Lou Ann Miller, Sanjaya Jayalath, and Ralph G. Nuzzo**

The field of 3D printing is an area of active research, with a substantial focus given to the design and construction of customized tools for applications in technology. There exists a particular need in these developing areas of opportunity for new multi-functional soft materials that are biologically compatible for the growth and directed culturing of cells. Herein, a composite material consisting of gold nanoparticles with useful plasmonic properties embedded within a highly hydrophilic poly-2-hydroxyethylmethacrylate matrix is described and characterized. This composite material serves dual functions as both host framework scaffold for cell lines such as pre-osteoblasts as well as a plasmonic biosensor for in situ measurements of living cells. The plasmonic properties of this system are characterized as a function of the material properties and related to compositional features of the material through a proposed light-directed mechanism. This chemistry provides a tunable, 3D printable plasmonic composite material of encapsulated gold nanoparticles in a biologically-compliant, acrylate-based hydrogel matrix. Surface-enhanced Raman scattering studies of 3D-microcultures supported by the scaffolds are carried out and the strong influence of perm-selective molecular diffusion in its analytical responses is established. Most notably, specific, largely hydrophilic, cellular metabolites are detected within the supported live cultures.

1. Introduction

Additive manufacturing, in particular 3D printing, provides a facile means of preparing with fine control a new series of soft material sensors, actuators, and mechano-chemical tools.[1–3] The current state-of-the-art facilitates high-level spatial and geometric control of printed materials of diverse form. Recent progress in research has seen traditional polymeric material classes being increasingly complimented by newer types of printable soft materials with attractive properties for incorporating and encoding programmable functions within the soft material matrix.[4,5] One especially active area of research in this regard relates to the development of materials to support and program the temporal development of cellular cultures in 3D ways that complement more traditional planar culturing methods of microbiology.[5–7] This work provides one element of support to address compelling opportunities for applications in regenerative medicine. A grand challenge with these types of emerging 3D cell cultures is to understand in a biologically-relevant way what factors drive cellular decision-making, directional growth and differentiation, and intercellular communication.[8,9] Such needs motivate the development of new analytical tools for use in studies of complex non-planar cellular cultures.

Gold nanoparticles are highly biocompatible and, when exploited with analytically sensitive surface-enhanced Raman spectroscopy (SERS) modality, can provide capabilities for spectroscopic sensing and chemically speciating markers of biological processes in ways suitable for use with living cellular cultures.[10,11] It well compliments other direct spectroscopic probes (e.g., mass spectrometry) that are of great current interest in research.[12,13] Enhancements of chemical signals have been reported up to a factor of 10^9 for molecules located near so-called "hot spots" on the plasmonic surface.[14] The enhanced electromagnetic field from plasmons account for a large portion of this enhancement.[15] Integrating plasmonically-active nanoparticles into a supporting material architecture suggests an intriguing approach to sensing that would be both biologically-compliant and

Dr. S. E. Lehman, Dr. J. M. McCracken, Dr. S. Jayalath, Prof. R. G. Nuzzo
Department of Chemistry
University of Illinois at Urbana Champaign
Urbana, IL 61801, USA
E-mail: r-nuzzo@illinois.edu
L. A. Miller
Frederick Seitz Materials Research Laboratory
University of Illinois at Urbana-Champaign
Urbana, IL 61801, USA
Prof. R. G. Nuzzo
Surface and Corrosion Science
School of Engineering Sciences in Chemistry
Biotechnology and Health
KTH Royal Institute of Technology
Drottning Kristinasväg 51, Stockholm 100 44, Sweden

The ORCID identification number(s) for the author(s) of this article can be found under https://doi.org/10.1002/adhm.202001040

DOI: 10.1002/adhm.202001040

 © 2020 Wiley-VCH GmbH

useful to investigation of cellular processes. Previous work has described non-hydrogel based sensing platforms including a chiral plasmonic substrate for interaction with living cells.[16] Generally in this work, cells are introduced directly to the substrate and allowed to freely interact. This provides useful opportunities to effect modifications of the substrate materials to control cellular attachment and growth but can also limit capabilities for sensing due to the fully exposed nature of the plasmonic substrate to the cellular culture environment.

Our work has generally focused on soft polymeric material substrates, such as 2-hydroxyethylmethacrylate (HEMA), which is exemplary as a class of materials that are biologically-compatible and afford useful functionality for use in biological devices or as an interfacial materials with biological systems.[17] The chemistry of this material is adaptable to 3D printing, allowing the fabrication of complex 3D form factor substrates for use in studies of cells in culture—a capacity we have demonstrated in earlier studies of programmable "4D" studies of cellular attachment, differentiation, and growth (i.e., with fibroblasts, pre-osteoblasts, and explants of the dorsal root ganglion taken from rats.[8,18] Osteoblasts (the cultures of which are studied here) are part of the bone remodeling cycle and have interesting cellular and built-in biological triggers that are highly chemoresponsive.[19] Pre-osteoblasts undergo differentiation into full osteoblasts before transforming into osteocytes, the active bone-depositing cellular machinery. These osteocytes undergo apoptosis, or programmed cell death, upon releasing the bone-forming components. Differentiated osteoblasts secrete both the protein matrix collagenic components as well as the mineralized hydroxyapatite ($Ca_{10}(PO_4)_6(OH)_2$) compositions comprising intact, mature bone.[20]

In this report, we describe a complex composite material for the fabrication by 3D printing of hydrophilic pHEMA structures with embedded gold nanoparticles generated via an in situ reduction process. The physicochemical and spectroscopic properties, as well as the in-vitro bioanalytical sensing capabilities of this composite material are described. The processing impacts on its utility as a biologically-compliant scaffold material for cellular growth and development is demonstrated using a bone-forming pre-osteoblast cell line, and its sensing properties exploited to measure signatures of cellular metabolism in living cells in situ in a discrete, non-invasive way.

2. Results and Discussion

2.1. Plasmonic Scaffold Printing and Development

The process of the scaffold synthesis and development is schematically shown in **Figure 1**a. The 3D printed ink material, a complex mixture of HEMA monomer, EGDMA crosslinker, Au-NP precursor, and pHEMA homopolymers of varied molecular weights, is cured through photoinitiated free-radical chemistry. This forms a tough, biologically-compatible hydrogel material that can be used for the growth and maintenance of cellular lines of interest. After the UV curing process, the material is exposed to a solution of sodium ascorbate, which elicits a redox reaction that reduces the auric ions (Au^{3+}) within the cured ink to form (as we show) highly dispersed/non-aggregated elemental gold in the form of nanoparticles. This in situ production of the gold nanoparticles has two main advantages over a direct incorporation of the NPs. First, it prevents the aggregation of gold nanoparticles during the various processing/printing steps of the hydrogel ink material. Second, as a particle free ink it prevents structural jamming via aggregation during printing, thus improving capabilities for high resolution printing—as illustrated in the current work via the exemplary extrusion of the HEMA/pHEMA hydrogel ink through a relatively small nozzle (i.e., 30 μm) at a moderate pneumatic pressure (≈20 psi), facilitating high control and structural fidelity of the 3D scaffolds.

False-color images of a printed structure are shown in Figure 1b during each stage of the process. False color images are created by assigning colors to grayscale pixels in images of each stage based on the intensity. Green colored areas represent low intensity areas in the grayscale image whereas orange color represent high intensity areas in the grayscale image. The true color changes associated with curing and development are more subtle in consequence of the extremely low mass fractions of Au used in the ink (Figure S1 in the Supporting Information shows a true-color image of a representative 3D-printed scaffold structure). In the current work, the pHEMA molecules contained in the ink provide the necessary rheological properties (i.e., viscosity) for filament extrusion. It is not robustly buildable at this stage of processing, however, and further modifications/post-print crosslinking steps as are discussed in detail in our earlier work must be adopted to enable more sophisticated forms of 3D fabrication.[8,18,21] The utility of this material as a spectroscopic probe of cells in culture does not require such higher levels of complexity to validate its utility, and demonstrations using simpler form factors were therefore adopted for subsequent study. An exemplary printed test structure is shown in the left panel of Figure 1c, colorized to demonstrate the typical appearance of the fully developed plasmonic scaffold. Here a serpentine pattern of loops and folds was employed to provide a large surface area of the material on which cell attachment can occur following explicit models employed in our earlier studies of cellular growth and direction.[8] A true-color image of part of the scaffold is shown in the middle panel of the Figure 1c, demonstrating the obvious plasmonic nanoparticles embedded in the material. The transmission electron micrograph of a thin film section in Figure 1c shows the physical morphology of the embedded gold nanoparticles grown in situ. Further details of the gold nanoparticle synthesis and analysis are described in the following sections.

2.2. Nanoparticle Synthesis Chemistry

We found in control studies that different thicknesses of the ink material, when cast as thin films (not shown), gave rise to materials post-development that were optically heterogeneous upon visual inspection. This degree of heterogeneity varied as a function of the material thickness, implying that different nanoparticle sizes were being formed in each case. To investigate this, materials were printed onto a quartz slide and monitored spectroscopically as a function of material processing conditions (**Figure 2**a) by measuring the extinction across the ultraviolet-visible range (200–800 nm) during each step of the process. A plot of the absolute extinction is available (Figure S2, Supporting Information).

© 2020 Wiley-VCH GmbH

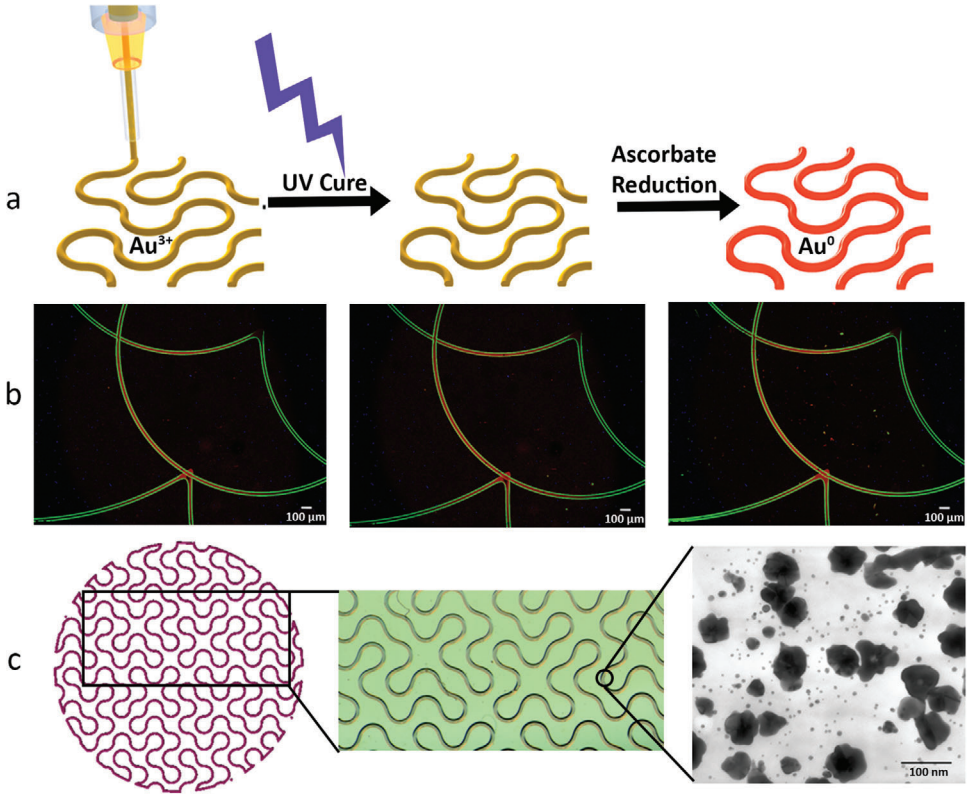

Figure 1. a) Schematic diagram of the material printing and development process. Printed ink is cured to cross-link the free acrylate groups by UV irradiation, then free auric (Au3+) ions are reduced to elemental gold (Au^0) by exposure to an aqueous ascorbate solution. b) False-color images of a printed object at each of the material processing steps. c) Colorized schematic of the serpentine pattern used as a biocompliant scaffold for cell culture growth and sensing, with a true color optical image of the post-processing (as described in (a)) scaffold with electron microscopy of the gold nanoparticles formed in situ during the reduction process, after the time delay

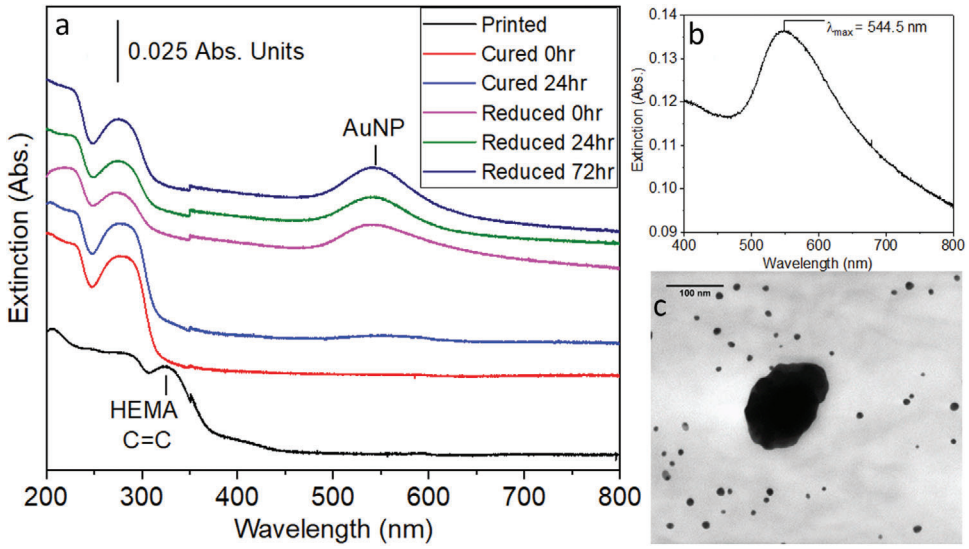

Figure 2. Materials characterization of the printed composites. a) Spectroscopic study of the development process. The initial alkene peak is visible after printing (≈340 nm), which disappears after curing. Growth of the characteristic plasmon for gold nanoparticles is visible around 550 nm following exposure to reductant. b) Localized surface plasmon resonance of the embedded gold nanoparticles. c) Single gold nanoparticle from transmission electron microscopy at high magnification. Scale bar 100 nm. Smaller seed particles of gold are visible, which likely result from the highly rapid processing during the ascorbate reduction step.

© 2020 Wiley-VCH GmbH

In the printed material a strong absorption feature at around 325 nm is observable which is due to the $\pi \rightarrow \pi^*$ transition associated with the alkene functionality in the free methacrylate monomer. This feature is absent in systems that have been UV irradiated owing to the chemical consumption of the alkene during the photopolymerization process. Even though there are no spectral features that can be observed in the visible range after the initial curing, a weak feature around 550 nm that can be ascribed to gold nanoparticles appeared when kept 24 h in the dark. Reduction of the Au^{3+} ion has been documented in the literature, a reaction occurring with the alkene moieties of the monomer as previously described.[22] This is a sensitivity similarly observed experimentally in the Au/HEMA ink, in that autocatalytic decomposition leading to Au NP formation becomes pronounced after ≈24 h even when stored under cold and dark conditions. The timing of the reduction step turns out to be the most critical parameter that ultimately determines the manner in which the formation of the gold nanoparticles proceeds within the polymer matrix. Based on the spectroscopic data available, an initial photoreduction of some of the Au^{3+} ions occurs during the UV curing step of the printed hydrogel. As a result, seed nanoparticles are formed within the gel matrix giving rise to the weak spectral feature around 550 nm after 24 h. Upon addition of the reductant, the seeds grow concurrently with chemical reduction of the Au^{3+} remaining in the cured polymer network. Ultimately, the initial seed formation determines the final nanoparticle size based on the initial irradiation conditions used during the curing process. The delay in the chemical reduction step serves to allow a chemical evolution of the nuclei for NP growth, which gives rise to asymmetric spheres if the reduction is done quickly (0 h wait) or raspberry-like particles if the reduction is delayed (72 h delay). This allows a degree of fine tuning of the NP morphology through controlled growth without the modification of the total amount of Au^{3+} ions present in the material. Although not investigated in detail here, the concentration of the gold salt provides an additional variable through which the plasmonic properties of the Au NPs can be tuned.

2.3. Material Characterization and Analysis

We carried out an extensive characterization effort to provide a comprehensive picture of the materials properties of the NP-embedded gel. The plasmonic properties of the nanoparticles were first analyzed via localized surface plasmon resonance spectroscopy (LSPR) to better understand their nature. The spectra were collected by mounting the reduced samples in the beam path and taking the bare glass as a 100%T sample for baseline correction. Using the conditions described above (24 h ripening delay), a plasmon peak appears at 544.2 nm (FWHM = 106 nm) as determined by a derivative analysis of the spectral data (Figure 2b). This frequency and line shape of this plasmon peak implies a size for the gold nanoparticles around 55 nm based on commonly reported results from the literature.[23] This was corroborated by TEM observations of thin sections made of the printed scaffolds following the reduction, as are discussed below.

To carry out the TEM measurements, cured gel filaments in their dehydrated state were embedded in epoxy as detailed above in the methods section. To facilitate imaging, the serpentine pattern described above was not used and instead a dense grid pattern of lines at the specified diameter (30 µm) were printed onto a sheet of Aclar fluoropolymer which had been rinsed with ethanol, then water, and dried fully. The Aclar sheet facilitated the lift-off of the printed material for the sectioning protocol. An electron micrograph of a NP material complimenting that shown in Figure 1c in Figure 2c. This shows the raspberry-like nature of the gold nanoparticles obtained after a 72-h reduction delay. A number of small (likely growth nucleating seed) nanoparticles can also be seen in the electron micrograph. We believe it likely that the smaller seeds seen here are formed in the photoinduced crosslinking step. Finally, it is of interest that the timing of the reduction step (immediately after the curing or delayed by 72 h) has no effect on the size of the nanoparticles formed even though it affects the nanoparticle morphology (Figure S3a,b, Supporting Information). This suggests that overall particle size is only controlled by the total amount of initial free Au^{3+} ions within the polymer matrix and does not depend on the time at which reduction occurs. Selected area diffraction was also employed to confirm the identity of the observed gold nanoparticles, whose assignment was established by the indexed reflections for the crystal planes of metallic Au (Figure S3c, Supporting Information).

2.4. Nanoparticle Reduction Control

To further explore and quantify the relationship between material thickness and the ultimate morphology of the gold nanoparticles formed (see above), a systematic study was carried out by printing sequential layers of the material and spectroscopically interrogating them. In this experiment, a set of prints that consist of one to four layers of the composite precursor ink was made in an "I" pattern on glass as shown in the SI (Figure S4, Supporting Information) and the plasmon peak measured as a function of the number of layers. Due to the intrinsic viscosity of the ink, profilometry was employed to empirically measure the height of the printed materials. The spectroscopic characteristics of the plasmon peaks obtained varied non-linearly across a series of up to four layers of material. The qualitative features evidenced by the spectroscopy involves changes in both line shapes, intensities, and peak frequencies as seen in the SI (Figure S5, Supporting Information). These data were fit to an empirical single exponential decay model, as shown in the SI. The experimental profilometry measurements are also given in the SI (Figures S6–S9, Supporting Information). Notable "double" plasmon were observed for prints formed by triple and quadruple filament overlays. These attributes are directly correlated with poor fidelity in the thickness throughout the print and thus a likely heterogeneity of size (i.e., red-shifted plasmons) in the NP structures formed. This further implicates the important role that diffusive accretion of Au^{3+} ions at the nuclei promoting growth plays in this system.

2.5. SERS Activity and the Hydrophilic Nature of the Composite

Gold nanoparticles have excellent sensing capabilities by SERS due to the localized surface plasmons they evince, which enhance the local electromagnetic field magnitudes present at their surfaces. As seen in the TEM images there are smaller (seed-like)

© 2020 Wiley-VCH GmbH

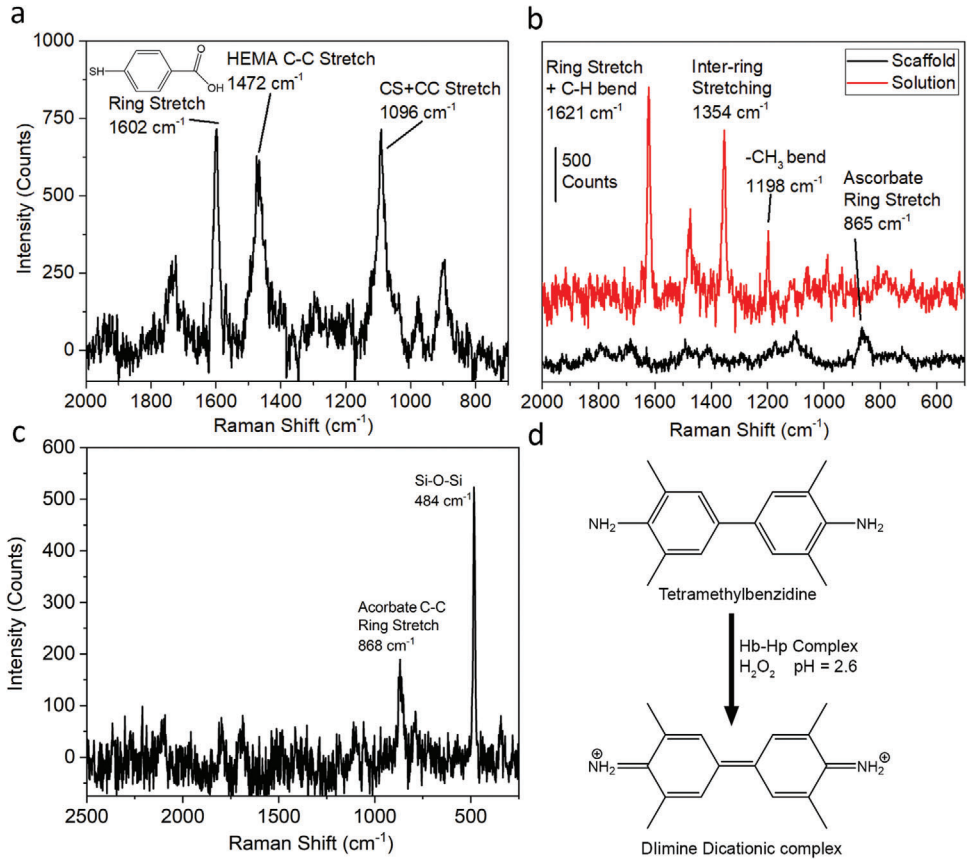

Figure 3. a) Surface-enhanced Raman spectroscopy shows characteristic strong signals for 4-mercaptobenzoic acid monolayers on the gold nanoparticle surface. b) A large dication of tetramethylbenzidine is not able to pass through the polymer network but is easily detected in solution on citrate-capped spherical gold nanoparticles. c) Control experiment of deionized water on the scaffold. A trace amount of ascorbate from the reduction process was detected. The feature around 480 cm^{-1} is due to the glass cover in place over the culture. d) Reaction schematic for the preparation of the diamine dicationic complex from tetramethylbenzidine catalyzed by hemoglobin–haptoglobin (Hb–Hp) complex.

gold nanoparticles that are also embedded in the polymeric matrix. Due to their known lower SERS enhancement factors, the laser excitation wavelength (532 nm) chosen was matched to the plasmon excitations of the larger (i.e., 50 nm) particles, as they have the highest theoretical enhancements under these conditions. [24–26] To evaluate their performance with the gel composite material, a baseline experiment was carried out to assess their activity in SERS. To do so, p-mercaptobenzoic acid (pMBA) was incubated with the printed, developed scaffold to form a self-assembled monolayer of the thiol on the surface of the gold nanoparticles and Raman spectroscopy measurements made to characterize them. Strong SERS signals corresponding to the NP-bound thiol were observed at 1602 (ring stretch) and 1096 cm^{-1} (CS + CC stretching) (**Figure** 3a). The two assigned peaks are notably blue-shifted when compared to those reported in the literature 1584 (ring) and 1075 (CS + CC) cm^{-1}) for molecules adsorbed onto gold nanoparticles in free solution.[27] Due to the hydrophobic nature of the aromatic ring in the probe molecule, a specific perturbation to these modes might arise due to the highly hydrophilic environment of the supporting gel matrix affecting orientational attributes of its binding/organization at the NP surface. Whatever the physical interactions of the probe molecules within the polymer network that result in the observed blue-shift, their large magnitude (≈20 cm^{-1}) indicates a strong interaction. Control experiments indicate that, in this instance, the interactions here are specifically influenced by the bonding of the pMBA adsorbates to the NPs. This is illustrated in the SERS responses seen for untreated scaffolds immersed in water (Figure 3c), which show only modes assignable to the bonding of a residual trace quantity of ascorbate on the NP surface.

We next explored other limits of SERS based sensing inconsequence of the interactions occurring between analyte molecules and the polymer network. These were explored using a tetramethylbenzidine dicationic complex, prepared from the catalytic reaction of the hemoglobin–haptoglobin complex.[28] This reaction proceeds via a two-electron reduction of the benzidine to yield the diimine complex under acidic conditions (to stabilize the diimine complex), with the hydrogen peroxide undergoing disproportionation to water and molecular oxygen in the process (Figure 3d). The TMB^{2+} complex interacts and binds easily to the surface of gold nanoparticles, giving rise to a measurable SERS spectrum for the cationic molecule. When 75 µL of the prepared complex was dropped onto the plasmonic scaffold and incubated at room temperature overnight, no peaks were detected in Raman spectra subsequently acquired that are assignable to the expected analyte.

© 2020 Wiley-VCH GmbH

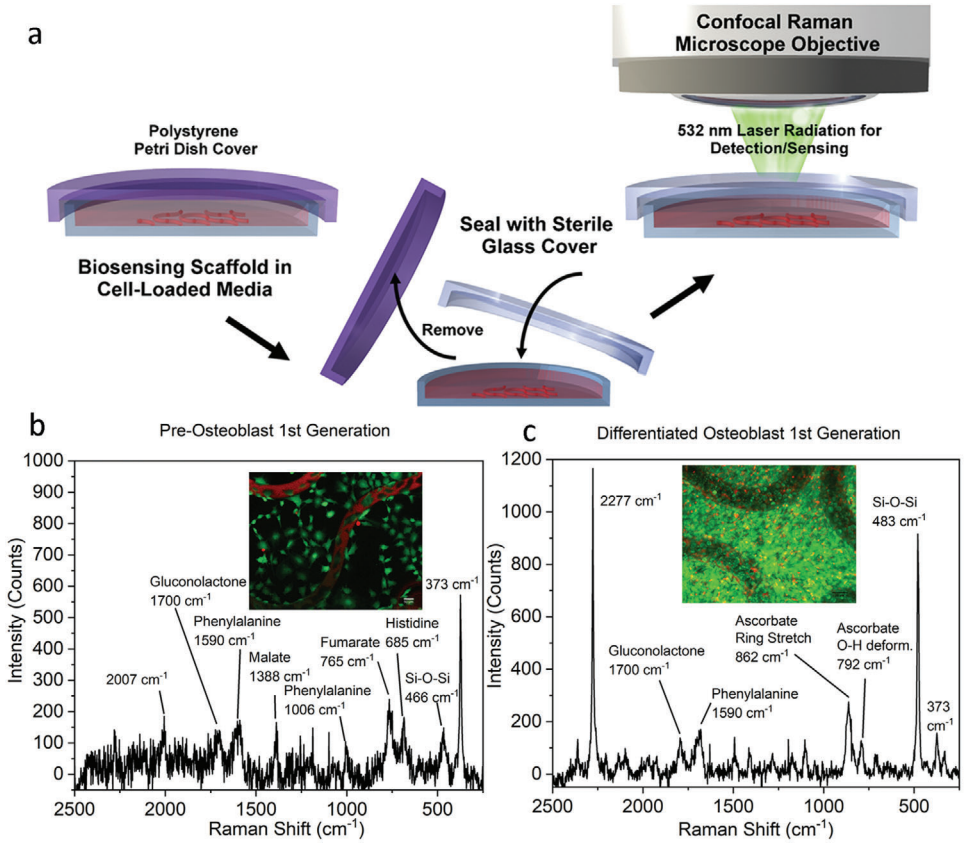

Figure 4. a) Schematic of the sterile transfer of living cellular culture for SERS. The optical objective both delivers and collects radiation during microscopic sensing. b) In situ SERS on pre-osteoblasts cultured on the plasmonic scaffolds during growth. c) In situ SERS on pre-osteoblasts cultured on the plasmonic scaffolds during post-differentiation. Characteristic Raman peaks for metabolites are detected. The inset images are composite live/dead images wherein green indicates living cells and red indicates dead. The peak at 373 cm^{-1} has been assigned to adsorbed hydroxide as described in text.

These modes, however, are easily detected upon addition of small amount of a colloidal AuNP suspension (prepared from a literature procedure using a buffered-citrate medium) (Figure 3b).[29] Given the abundance of available oxygen atoms for coordination, it was expected that the cationic complex would diffuse into the polymer network. However, this was not observed during the above experiment. This suggests that the cationic TMB^{2+} complex is not taken up easily within the hydrophilic network of the polymeric gel. The mesh size of the hydrogel network seems unlikely to be a causative factor underlying this apparent permselective behavior. While smaller effective pores might prevent the absorptive uptake of larger molecules into the polymeric network, it seems likely that a more complex osmotic preclusion operates within the composite polymer/nanoparticle material, one that functions similar to a selectively permeable membrane. This has critical implications for the nature of the spectroscopy implemented during the use of the material as a scaffold for cellular cultures.

2.6. Spectroscopic Speciation of Cellular Analytes

Systems closely related to the composite material examined in this study have been examined in earlier work as a printable scaffold material for the support of 3D cellular cultures,[8,18] and here in extension are investigated as well as a spectroscopically active sensing platform. Murine osteoblasts were utilized as a test culture to explore this functionality. The cells were seeded directly onto sterilized composite scaffolds and grown according to procedures that have been described in previous studies from our group on printable pHEMA materials.[8] As a benchmark for the system integrating embedded Au NPs, LIVE/DEAD assays were carried out to verify the biological compatibility of the gel with pre-osteoblasts grown in culture (**Figure 4**, spectral insets). Based on the LIVE/DEAD assay results, no difference in the viability and progression of growth of the cells is found on the composite material when compared against the closely-related nanoparticle-free material discussed in McCracken et.al, 2016. Additional LIVE/DEAD assay images are given in Figures S10–S12, in the Supporting Information, representing three different stages of the cell growth: 3 days after seeding; 7 days after seeding (post-differentiation); 28 days after seeding (post-differentiation). This is an expected result following the well-understood biological compatibility of elemental gold, and compares favorably to other plasmonic materials such as Ag that more easily undergo dissolution processes that release potentially cytotoxic levels of dissolved metal ions.[30] More notable, though, is the fact that the nanoparticles are

© 2020 Wiley-VCH GmbH

Table 1. Full assignments of the SERS spectrum of cell metabolites (Figure 4b,c).

Raman Shift [cm^{-1}]	Vibrational Mode	Assignment	Chemical Structure
685	$\delta(CO_2)$	Histidine[29]	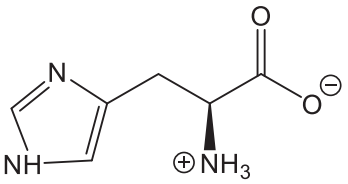
765	ω(OH)	Fumarate[28]	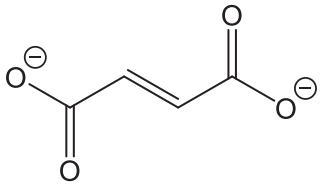
1006	Ring stretch	Phenylalanine[30]	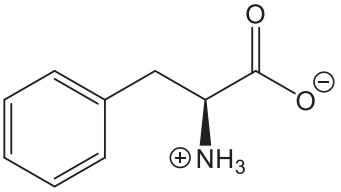
1388	ν (C–O) + δ(O–H)	Malate[27]	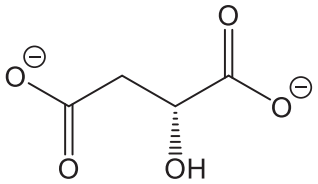
1590	ν (C=O)	Phenylalanine[30]	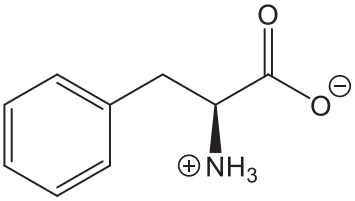
1700	C=O stretch	Gluconolactone[26]	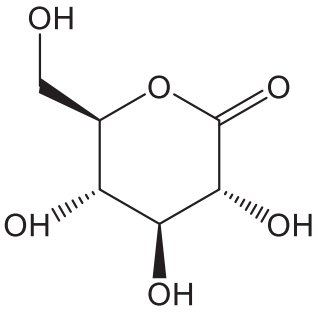

encapsulated within the polymer matrix and thus the cells do not directly contact the nanoparticle surfaces.

The live-cell spectroscopic studies were carried under sterile conditions as shown schematically in Figure 4a. All exposures of the cellular culture outside the incubator were minimized to preserve viability. The most sensitive step involved the replacement of the polystyrene culture cap with a glass cover to circumvent contributions from its interfering Raman bands for the duration of the spectroscopic measurements as represented in the schematic. Strong Raman signals are seen in each case (Figure 4 and **Table 1**) with an additional peak ascribed to adsorbed hydroxide as previously reported by others.[31] The SERS

© 2020 Wiley-VCH GmbH

data recorded after the culture reached confluence (Figure 4b) show strong features assignable to specific species associated with cellular metabolism—modes for gluconolactone,[32] malate,[33] fumarate,[34] histidine,[35] and phenylalanine[36] being most prominent. It is an interesting feature of the current data that as in the control experiments discussed above it is largely small/hydrophilic molecules that stand out as detectable analytes in the SERS experiment. It is particularly striking that peaks ascribable to the amide bands of proteins (≈1600 cm^{-1}) are not observed, even though they are widely abundant in the culture medium. This observation follows the correlation of impacts due that result from both a sterically and osmotically mediated perm-selectivity for small polar analytes that the pHEMA matrix appears to afford the Au NPs.

We now consider the SERS data obtained after the culture was switched to osteoconductive conditions (Figure 4c). Several modes seen prior to differentiation appear in these data as well (gluconolactone[32] and phenylalanine[36] being most prominent along with modes assignable to ascorbate). Although the mineralization mechanism seen at this stage is not completely understood, recent work suggests that complex transport-mediated processes are likely involved. The chemically congruent deposition, in conjunction with co-deposited proteins, follows the general overall equation[20]

$$6HPO_4^{2-} + 2H_2O + 10Ca^{2+} \rightleftharpoons Ca_{10}(PO_4)_6(OH)_2 + 8H^+$$

As acid is formally produced, active cellular mediation in the local environment is required to maintain physiological conditions.[37] The mode seen at 373 cm^{-1} (assigned to adsorbed OH^- at the NP surface) follows a local OH^- concentration that is expected to be higher than that of the bulk solution due to the physiological requirements for mineralization.[38,39] Some cell death (as expected) is noted due to the change in the culture medium (as corroborated by the results of LIVE/DEAD assays carried out after 21 days post-differentiation (Figure 4, right panel, inset). These images also reveal the complex material compositions of collagen and biogenic hydroxyapatite that result from the elicited biomineralization process (Figure S14, Supporting Information). We note that origin of the high intensity Raman mode appearing at 2277 cm^{-1} is not understood at present (to our knowledge there are no chemical species commonly associated with mammalian cellular cultures that would produce a Raman signal in this region, one known as cell-silent Raman window that spans from 1800–2600 cm^{-1}).[40,41] Control experiments further serves to support above assignments . Spectral analysis in this case reveals phosphate (P-OH stretch) and chloride (Au-Cl stretch), which are abundant in the culture medium, being adsorbed onto the gold nanoparticle surface.[42,43]

The study described here demonstrates the viability of bioanalytical spectroscopic sensing of live-cell cultures using gel scaffolds that embed plasmonic NPs. The current work illustrates a synergistic approach to enabling cell growth and detection of specific analytes concurrently. It further compliments approaches that more typically introduce free nanoparticles to cells within the solution phase ambient for spectroscopic detection.[44] That approach facilitates detection, but requires introduction of a non-endogenous agent to the cells. Such an approach is also less than ideal as it represents a perturbation to the biological system with somewhat unknown (and likely highly complex) effects. Other approaches have implemented introduction of cell cultures to nanoparticle suspensions after killing the cells, but this is clearly limited to single time-point measurements along the growth and life cycle.[45]

New approaches to implement SERS-based microscopy have also been developed-in contrast to traditional fluorescence imaging-but again suffer from the necessity of introducing (functionalized) SERS substrates, i.e., nanoparticles, into the cellular culture medium prior to the spectroscopic detection/imaging.[46] The materials described here preclude the need to provide viable forms of cell contact or trans-membrane transport to conduct model assays by SERS. The limitation of our approach (vide supra) is that the hydrogel containment necessarily acts as a sieving mechanism to direct and control diffusion to the nanoparticle surface. However, it also provides some benefits by preventing the adsorption of proteins on gold nanoparticles. Generally, when introduced to cell cultures as a SERS probe AuNPs non-specifically absorb proteins as a corona that hinders the detection of cellular metabolites of interest and requiring complex surface modifications to prevent their formation.[47] The in situ gold nanoparticle generation method used in this study provides a simple yet powerful solution for this critical issue by preventing the proteins from reaching the gold nanoparticle surface. A drawback of this perm-selective substrate is that a large number of biological molecules of interest are likely excluded from detection, even though they may be present in sufficient concentrations, due to the nature of the host polymeric hydrogel network. This type of composite material thus has both positive and negative aspects to its implementation as a SERS-active substrate for biological growth, but nonetheless one that functions perpendicular to other approaches previously carried out in this space. It seems likely, however, that with careful molecular design, the physicochemical attributes that mediate the perm selective behaviors noted here might be tuned to more broadly enable useful forms of live-cell bioanalytical measurements.

3. Conclusions and Future Work

This report demonstrates a new composite material capable of a high level of tunable control for use in spectroscopic investigations of cellular cultures supported on printed gel scaffolds. The capacities for modification in terms of the in situ synthesis of gold nanoparticles the serve as integrated plasmonic sensors are quite general and compliment requirements needed to support printing-based modes of fabrication. Finer structured materials than the ones employed here are theoretically possible with a particle-free ink such as the one studied herein. A high level of mechanical control over the physical processing and printing of the hydrogel ink material enables custom geometric designs of high structural fidelity. This composite material is shown to be hydrophilic and in consequence usefully perm-selective. A clear affinity as a biological growth platform is demonstrated and cellular sensing is carried out on live cells while maintaining a sterile field for further studies. Future work should include the examination of the porous nature of the scaffold and its necessary implications for bioanalytical applications, as well as a more expansive study of how the gel composition and structure can be manipulated to improve specific signal recognition against

© 2020 Wiley-VCH GmbH

complex background interferences. A final avenue of interest would be to explore how the material evolves over time upon continued cell growth/media exposure, as it may undergo dynamic changes in terms of the nanoparticles or the polymer itself at the liquid-solid interface over extended time scales. Overall, this type of composite scaffold should facilitate enhanced types of biologically-compliant 3D printed materials that are multifunctional and highly versatile for desired applications in chemical sensing, as well as new types of relevant bionanomaterials.

4. Experimental Section

Ink Preparation and Printing: A base 2-hydroxyethylmethacrylate (HEMA) ink was prepared by mixing the following in a glass scintillation vial: deionized water (2.45 g), HEMA monomer (4.0 g) (Sigma), ethyleneglycoldimethacrylate (0.1 g) (inhibitors removed, Sigma), Irgacure 2959 (50 mg) (Sigma), pHEMA (1.0 g, 1 000 000 g mol^{-1} MW, Sigma), pHEMA (2.5 g, 300 000 g mol^{-1} MW, Sigma). The material was homogenized in a Thinky (ARE-310) mixer for 5 min at 2000 rpm. The material was held at 4 °C in the dark for seven days and was physically stirred every day to promote complete dissolution to give a homogeneous, clear gel. To prepare the Au/HEMA ink, a solution of $AuCl_3 \bullet 3H_2O$ (760×10^{-3} M) was prepared in deionized water. An aliquot of the base ink (0.600 g) was combined with of the gold (III) chloride solution (25 µL) in a scintillation vial. The material was briefly mixed for two min in the Thinky mixer to give a yellow, homogeneous gel. The glass vial was cooled under running cold tap water immediately following the mixing protocol to limit thermally driven polymerization.

This material was transferred to a plastic syringe loaded into a custom-built 3D printer utilizing a pneumatic extruder (Ultimus V and HPx High-Pressure Dispensing Tool, Nordson EFD) mounted to an *X–Y–Z* motion controller (AGS-1000, Aerotech Inc., Pittsburgh, PA). The syringe was equipped with a 30 µm diameter glass tip (Nordson EFD) and printed at a linear rate of 1 mm s^{-3} using an appropriate pneumatic pressure to deliver a continuous flow of ink. Materials were printed on glass slides that had been functionalized by incubating them in a (2:2:1) mixture of water, glacial acetic acid, and trimethoxysilylpropylmethacrylate for 30 min.

AuHEMA Composite Development: Once printed, the composite ink was cured via exposure to a UVP 365 nm UV lamp, 100 W for 2 h. The material was held for up to 72 h in the dark at room temperature, and then the cured materials were immersed in a 5×10^{-3} M aqueous solution of sodium L-ascorbate overnight to allow for the reduction of the Au^{3+} ion to form Au nanoparticles in situ. The material was then transferred into deionized water changed thrice over the course of 12 h to remove any residual ascorbate within the polymer matrix. The glass slide was cut into individual scaffolds, which were then glued onto Petri culture dishes using a standard hot-glue gun.

Materials Characterization: Optical imaging was carried out using an Olympus SX7 Microscope with a DP25 Camera and a white light source (Optical Analysis Corporation). Localized surface plasmon resonance spectroscopy was done using a non-dispersive Cary UV–vis Spectrophotometer equipped with a solid-state acquisition apparatus for mounting of samples. Materials were taped into place in a vertical position in the spectrometer utilizing a metal plate with a 4.0 mm circular aperture in the middle to allow transmission of the incident radiation. Data was collected across the visible range (400–800 nm) on glass substrates or across the UV–vis range (200–800 nm) on quartz substrates at a linear scan rate of 100 nm min^{-3}.

Due to the nature of the hydrogel as an insulator, microtome sectioning was carried out to prepare the materials for transmission electron microscopy. In order to enable electron microscopy, materials were 3D printed as described above onto a sheet of Aclar fluoropolymer. The material was cured and developed using 5×10^{-3} M ascorbate as described above. Then the material was prepared for embedding into liquid epoxy resin by first treating with 2% aqueous osmium tetroxide for two hours at 4 °C followed by rinsing and enbloc staining with 7% aqueous uranyl acetate for two hours at 4 °C in the dark to improve contrast. This was followed by dehydration of the hydrogel using sequential washes of 25, 50, 75, 95, and 100% ethanol (with the remaining proportion water) for 15 min each. A wash of acetonitrile for 15 min was used to remove any residual ethanol from the specimen. Then the sample was infiltrated with 1:1 and then 4:1 epoxy: acetonitrile, then pure epoxy resin across several days and cured at 80 °C to make the final cuttable blocks. The sample was loaded into the epoxy such that it would result in a face-on orientation upon curing/hardening. This was done so that the material could be cut across the breadth of the structure. Sectioning was done using a diamond knife on a Reicher Ultracut E ultramicrotome. Sections (≈80–100 nm thickness) were then picked up onto copper TEM grids and held under a 70 W light bulb until the section was dry. TEM grid/materials were carbon-coated using a Cressington Carbon Coater 108A sputter coater and a graphite rod as carbon source by applying 4.2 V across the rod for 10 s. This was done to give a very light coating of carbon on the materials to reduce/eliminate charging on the material. Transmission electron images were collected using a JEOL 2010F Transmission Electron Microscope equipped with a W or LaB_6 filament source. Micrographs were captured by using Kodak 4489 EM film using a two second exposure. The film was then developed according to the manufacturer's protocol. The developed photographs were scanned in at high resolution to produce the electron micrographs.

Particle sizing was done by counting particle diameters in ImageJ (N = 32 particles) and graphing the data as a histogram in Origin 9.1 software. A Gaussian curve was fit to the data to determine the center of the distribution, which was taken to be the average particle size. Selected area diffraction (SAED) was carried out using the same electron microscope setup as described above by viewing the diffracted beam through a 200 nm aperture to isolate a single particle. The diffracted beam was then imaged directly using a CCD camera. Profilometry was done on the printed materials using an LSM 800 3D Optical Profiler (Zeiss).

Cellular Growth and Maintenance: Pre-osteoblasts (MC3T3-E1 Subclone 4, Mus musculus, ATCC) maintained prior to use above liquid nitrogen vapor (≈100 K) were grown in a complete medium consisting of Alpha Minimum Essential Medium (-Ascorbate) with 10% fetal bovine serum (ATCC) and penicillin-streptomycin (100 U mL^{-1}). Cells were grown and maintained at 37 °C/5% CO_2 in a water-jacketed incubator. Upon growth to confluence in a plastic culture bottle 75 cm^2 the cells were dissociated by first rinsing with sterile phosphate-buffered saline (PBS, 3 mL, pH = 7.4) and then incubated at 37 °C with 0.25% trypsin-EDTA (3 mL, Gibco) for 15 min, in which dissociation was confirmed by microscopic examination. Upon sufficient dissociation, the complete media (4 mL) was added to neutralize the trypsin, then the cell suspension was transferred to a sterile 15 mL conical centrifuge tube. Approximately 2 mL of media was used to rinse the cell culture out and this aliquot was also added to the 15 mL conical tube as well. The cells were centrifuged at 500 g for 10 min to gently pellet the cells. Almost all of the media was removed and replaced with fresh complete media (1.00 mL) at 37 °C. The tube was gently shaken by hand to suspend the cells and the cell suspension (300 µL) was added onto scaffolds that had been sterilized by exposure to UV radiation for a minimum of two hours. An additional 2–3 mL of complete media was added to the scaffolds to ensure sufficient growth conditions. Cells were maintained in the incubator at 37 °C/5% CO_2 and media exchanged every third day. Differentiation media was prepared via supplementing the normal media described above with filter-sterilized (0.22 µm) solutions of β-glycerolphosphate and ascorbic acid in the minimum essential medium to supplement the growth medium to final concentrations of 10×10^{-3} M and 50×10^{-6} M, respectively. Transfers of all biological components were carried out aseptically in a biological hood. A live/dead assay was carried out using a Mammalian LIVE/DEAD Viability Kit (Invitrogen) using calcein-AM and homoethidium dimer as stains. The two frozen stains were thawed in the dark at room temperature, and then each stain (5 µL) was added into sterile Dulbecco's phosphate buffered saline (10 mL) at room temperature. The solution was gently mixed by inversion to completely homogenize it. Culture medium was removed from the cells in the biological hood and then the staining medium was added to cover the culture dish (3 mL each). The stain was allowed to penetrate into the cells

© 2020 Wiley-VCH GmbH

for 30 min at room temperature prior to imaging. Imaging was carried out on a Zeiss Axiovert 25 inverted microscope equipped with fluorescence filters. To visualize the calcein-stained cells (live) a filter at 494 nm was used for excitation, whereas to visualize the homoethidium-stained cells (dead) a filter at 528 nm was used. Composite images were prepared by merging red and green channels in ImageJ.

Spectroscopic Raman Sensing: Cellular cultures or other scaffolds of interest were aseptically transferred into a biological hood prior to Raman spectroscopy. A glass Petri dish cover that had been sterilized by spraying with ethanol solution (70%) which had been allowed to dry in the biological hood was swapped out for the plastic Petri dish cover within the biological hood. The sterile glass cover was held in place and taped to the culture dish to give a sealed sterile environment for spectroscopy. This entire construction was then transferred into a commercial Nanophoton Raman Microscope using a 5× objective. A green laser ($\lambda = 532$ nm) was used to probe the materials owing to the proximity to the measured plasmon of the gold nanoparticles. The instrument (CCD detector) was calibrated using standard emission lines from an internal helium lamp. A very low power (≈0.001 mW) was spread out in *X*–*Y* averaging mode across a 1.5 mm^2 area to ensure that the cell viability was not lowered due to excessive irradiation. Data was accumulated for 15 s with four individual spectra averaged to give the resulting spectra. Data was baseline corrected in OriginPro 2016 using a 16 point baseline.

Statistical Analysis: Particle size analysis of the gold nanoparticles was carried out using measurements in ImageJ to measure the nanoparticle diameter. A total of $N = 32$ particles at each condition (0 or 72 h) were measured and then tabulated in Origin 9.1 The data was plotted (as shown) as a histogram and fitted with the internal Gaussian function to determine the center of the fitted curve. This fitted center (given by Origin) plus/minus the standard error determined by the fit is reported in the Supporting Information and is shown overlaid on the histogram. No statistical analysis was used to differentiate between the observed values of the center of the function. All Raman/SERS spectra were manually baseline corrected in Origin 9.1 to remove the continuum fluorescence background, giving the reported spectra.

Supporting Information

Supporting Information is available from the Wiley Online Library or from the author.

Acknowledgements

S.E.L. wishes to thank Dr. Mikayla A. Yoder at UIUC for the profilometry data of the multilayers, Dr. Wacek Swiech in the MRL for assistance with collecting the diffraction patterns, Dr. Arif Z. Nelson for imaging some of the large printed materials, and Dr. Brittany Rauzan for helpful discussions. The authors gratefully acknowledge funding in the form of an Army Research Office MURI (W911NF-17-1-0351) for their support of this work. Experiments were carried out in part in the Frederick Seitz Materials Research Laboratory Central Research Facilities, University of Illinois at Urbana-Champaign.

Conflict of Interest

The authors declare no conflict of interest.

Keywords

3D printing, bio-compliant, biomimetics, gels, plasmonic sensing, SERS

Received: June 19, 2020
Revised: August 24, 2020
Published online:

[1] M. Banna, K. Bera, R. Sochol, L. Lin, H. Najjaran, R. Sadiq, M. Hoorfar, *Sensors* **2017**, *17*, 1336.
[2] J. Guo, R. Zhang, L. Zhang, *ACS Macro Lett.* **2018**, *7*, 442.
[3] M. Schaffner, J. A. Faber, L. Pianegonda, P. A. Rühs, F. Coulter, A. R. Studart, *Nat. Commun.* **2018**, *9*.
[4] Q. Fu, E. H. H. Wong, J. Kim, J. M. P. Scofield, P. A. Gurr, S. E. Kentish, G. G. Qiao, *J. Mater. Chem. A* **2014**, *2*, 17751.
[5] X. Yang, G. Liu, L. Peng, J. Guo, L. Tao, J. Yuan, C. Chang, Y. Wei, L. Zhang, *Adv. Funct. Mater.* **2017**, *27*, 1703174.
[6] Z. Tan, T. Liu, J. Zhong, Y. Yang, W. Tan, *J. Biomed. Mater. Res., Part A* **2017**, *105*, 3281.
[7] R. Edmonson, J. J. Broglie, A. F. Adcock, Y. Yang, *Assay Drug Dev. Technol.* **2014**, *12*, 207.
[8] J. M. McCracken, A. Badea, M. E. Kandel, A. S. Gladman, D. J. Wetzel, G. Popescu, J. A. Lewis, R. G. Nuzzo, *Adv. Healthcare Mater.* **2016**, *5*, 1025.
[9] K. F. Lei, C.-H. Chang, M.-J. Chen, *ACS Appl. Mater. Interfaces* **2017**, *9*, 13092.
[10] C. L. Haynes, A. D. McFarland, R. P. Van Duyne, *Anal. Chem.* **2005**, *77*, 338 A.
[11] J. Liu, C. Cai, Y. Wang, Y. Liu, L. Huang, T. Tian, Y. Yao, J. Wei, R. Chen, K. Zhang, *Adv. Sci.* **2020**, *7*, 1903730.
[12] C. Pei, C. Liu, Y. Wang, D. Cheng, R. Li, W. Shu, C. Zhang, W. Hu, A. Jin, Y. Yang, *Angew. Chem., Int. Ed.* **2020**.
[13] L. Huang, L. Wang, X. Hu, S. Chen, Y. Tao, H. Su, J. Yang, W. Xu, V. Vedarethinam, S. Wu, *Nat. Commun.* **2020**, *11*, 3556.
[14] H. Liu, L. Zhang, X. Lang, Y. Yamaguchi, H. Iwasaki, Y. Inouye, Q. Xue, M. Chen, *Sci. Rep.* **2011**, *1*, 112.
[15] G. C. Schatz, R. P. Van Duyne, in *Handbook of Vibrational Spectroscopy*, (Eds: J. M. Chalmers, P. R. Griffiths), John Wiley & Sons, Chichester **2002**.
[16] X. Zhao, L. Xu, M. Sun, W. Ma, X. Wu, C. Xu, H. Kuang, *Nat. Commun.* **2017**, *8*, 2007.
[17] Y. Zhang, D. Chu, M. Zheng, T. Kissel, S. Agarwal, *Polym. Chem.* **2012**, *3*, 2752.
[18] A. Badea, J. M. McCracken, E. G. Tillmand, M. E. Kandel, A. W. Oraham, M. B. Mevis, S. S. Rubakhin, G. Popescu, J. V. Sweedler, R. G. Nuzzo, *ACS Appl. Mater. Interfaces* **2017**, *9*, 30318.
[19] M. Ferron, J. Wei, T. Yoshizawa, A. D. Fattore, R. A. DePinho, A. Teti, P. Ducy, G. Karsenty, *Cell* **2010**, *142*, 296.
[20] H. C. Blair, Q. C. Larrouture, Y. Li, H. Lin, D. Beer-Stoltz, L. Liu, R. S. Tuan, L. J. Robinson, P. H. Schlesinger, D. J. Nelson, *Tissue Eng., Part B* **2017**, *23*, 268.
[21] J. M. McCracken, B. M. Rauzan, J. C. E. Kjellman, M. E. Kandel, Y. H. Liu, A. Badea, L. A. Miller, S. A. Rogers, G. Popescu, R. G. Nuzzo, *Adv. Healthcare Mater.* **2019**, *8*, 1800788.
[22] N. Savjani, D.-A. Rosca, M. Schormann, M. Bochmann, *Angew. Chem., Int. Ed.* **2013**, *52*, 874.
[23] S. Link, M. A. El-Sayed, *J. Phys. Chem. B* **1999**, *103*, 4212.
[24] S. Hong, X. Li, *J. Nanomater.* **2013**, *2013*, 790323.
[25] S. E. J. Bell, M. R. McCourt, *Phys. Chem. Chem. Phys.* **2009**, *11*, 7455.
[26] J. D. Driskell, R. J. Lipert, M. D. Porter, *J. Phys. Chem. B* **2006**, *110*, 17444.
[27] Y. Wang, W. Ji, H. Sui, Y. Kitahama, W. Ruan, Y. Ozaki, B. Zhao, *J. Phys. Chem. C* **2014**, *118*, 10191.
[28] J. Perumal, G. Balasundaram, A. P. Mahyuddin, M. Choolani, M. Olivo, *Int. J. Nanomed.* **2015**, *10*, 1831.
[29] F. Schulz, T. Homolka, N. G. Bastús, V. Puntes, H. Weller, T. Vossmeyer, *Langmuir* **2014**, *30*, 10779.
[30] X. Li, J. J. Lenhart, *Environ. Sci. Technol.* **2012**, *46*, 5378.
[31] C.-Y. Li, J.-C. Dong, X. Jin, S. Chen, R. Panneerselvam, A. V. Rudnev, Z.-L. Yang, J.-F. Li, T. Wandlowski, Z.-Q. Tian, *J. Am. Chem. Soc.* **2015**, *137*, 7648.

 © 2020 Wiley-VCH GmbH

[32] G. Jia, S. Qiu, L. G., J. Zhou, Z. Feng, C. Li, *Sci. China, Ser. B: Chem.* **2009**, *52*, 552.
[33] H. Baranska, J. Kuduk-Jaworska, R. Szostak, A. Romaniewska, *J. Raman Spectrosc.* **2003**, *34*, 68.
[34] J. D. Gelder, K. D. Gussem, P. Vandenabeele, L. Moens, *J. Raman Spectrosc.* **2007**, *38*, 1133.
[35] J. L. B. Faria, F. M. Almeida, O. Pilla, F. Rossi, J. M. Sasaki, F. E. A. Melo, J. M. Filho, P. T. C. Freire, *J. Raman Spectrosc.* **2004**, *35*, 242.
[36] G. Zhu, X. Zhu, Q. Fan, X. Wan, *Spectrochim. Acta, Part A* **2011**, *78*, 1187.
[37] C. R. Redhead, P. F. Baker, *Calcif. Tissue Int.* **1988**, *42*, 237.
[38] B. Marelli, C. E. Ghezzi, Y. L. Zhang, I. Rouiller, J. E. Barralet, S. N. Nazhat, *Biomaterials* **2015**, *37*, 252.
[39] Q. C. Larrouture, D. J. Nelson, L. J. Robinson, L. Liu, I. Tourkova, P. H. Schlesinger, H. C. Blair, *Physiol. Rep.* **2015**, *3*, e12607.
[40] F. Hu, S. D. Brucks, T. H. Lambert, L. M. Campos, W. Min, *Chem. Commun.* **2017**, *53*, 6187.
[41] Z. Zhao, Y. Shen, F. Hu, W. Min, *Analyst* **2017**, *142*, 4018.
[42] G. Niaura, A. K. Gaigalas, A. L. Vilker, *J. Phys. Chem. B* **1997**, *101*, 9250.
[43] Y. Peng, Z. Niu, W. Huang, S. Chen, Z. Li, *J. Phys. Chem. B* **2005**, *109*, 10880.
[44] A. Calvet, A. G. Ryder, *Anal. Chim. Acta* **2014**, *840*, 58.
[45] A. B. Veloso, J. P. F. Longo, L. A. Muehlmann, B. F. Tollstadius, P. E. N. Souza, R. B. Azevedo, P. C. Morais, S. W. da Silva, *Sci. Rep.* **2017**, *7*, 7175.
[46] M. Navas-Moreno, M. Mehrpouyan, T. Chernenko, D. Candas, M. Fan, J. J. Li, M. Yan, J. W. Chan, *Sci. Rep.* **2017**, *7*, 4471.
[47] S. Sloan-Dennison, M. R. Bevins, B. T. Scarpitti, V. K. Sauvé, Z. D. Schultz, *Analyst* **2019**, *144*, 5538.

© 2020 Wiley-VCH GmbH